ChemComm

COMMUNICATION

View Article Online
View Journal | View Issue

Cite this: *Chem. Commun.*, 2020, **56**, 3793

Received 26th December 2019,
Accepted 21st February 2020

DOI: 10.1039/c9cc09988c

rsc.li/chemcomm

Energy-resolved distribution of electron traps for O/S-doped carbon nitrides by reversed double-beam photoacoustic spectroscopy and the photocatalytic reduction of Cr(VI)†

Chitiphon Chuaicham, [a] Sekar Karthikeyan, [a] Radheshyam R. Pawar, [a] Yihuang Xiong, [b] Ismaila Dabo, [b] Bunsho Ohtani, [c] Yoonyoung Kim, [de] Jun Tae Song, [de] Tatsumi Ishihara [de] and Keiko Sasaki *[ac]

We report for the first time to our knowledge the identification of heteroatom-doped and undoped C_3N_4 with the energy-resolved distribution of electron traps (ERDT) near the conduction band bottom position (CBB) using reversed double-beam photoacoustic spectroscopy. The ERDT/CBB pattern is used to classify the type of elemental doping in C_3N_4, related to photocatalytic efficiency.

Identification, together with detailed determination of structures and developed material nomenclature, is the area most focused on in various research fields to investigate the properties of unknown materials. One of the most common analysis techniques used to examine the bulk properties of solid materials, powder X-ray diffraction (PXRD), distinguishes between the crystalline and amorphous phases and determines elemental compositions in developed materials. Fourier-transform infrared spectroscopy (FTIR) is a technique used to obtain an infrared absorption or emission spectrum of solid materials that provides information about functional groups and covalent bonds present in the materials. Brunauer–Emmett–Teller (BET) theory aims to explain the physical adsorption of gas molecules on a solid surface and serves as the basis for measuring specific surface area particle sizes and may provide some information about the structural or textural properties of the developed materials. However, in many material applications, the surface properties of advanced materials have a significant influence on the activities and efficacy with regards to relevant applications. In particular, in photocatalysis, surface electronic properties, such as the charge transfer through and electronic properties of the surfaces of solid materials, are essential in understanding specific photocatalytic mechanisms. Hence, it is necessary to identify the surface electronic properties of the solid photocatalyst using electrochemical techniques.

Recently, Ohtani *et al.* developed a novel analytical method, reversed double-beam photoacoustic spectroscopy (RDB-PAS), for measuring the energy-resolved distribution of electron traps (ERDT). The principles of and detailed information regarding advanced RDB-PAS techniques are narrated in a previous report.[1] The RDB-PAS technique successfully identified the surface properties of many photocatalysts and most of the metal-oxide powder samples under study.[1–3] Fingerprint ERDTs combined with conduction band bottom position (CBB) patterns may be useful in the correct identification of the surfaces of solids (electronic properties).

In this study, undoped C_3N_4, O-doped C_3N_4, and S-doped C_3N_4 samples were synthesized, using diverse precursors, for the photocatalytic reduction of Cr(VI) to Cr(III) under visible light irradiation. The guest elements O and S in the precursors (Fig. S1, ESI†) can be doped into the C_3N_4 structure during synthesis. The products obtained from melamine, dicyandiamide, urea, cyanuric acid, thiourea, and ammonium thiocyanate as precursors were denoted CMA, CDM, CU, CCA, CT, and CAT, respectively. Moreover, the product of calcination of melamine in a N_2 flow was also prepared, denoted as CMN. In the primary stages of this research, we observed that the typical PXRD and FTIR methods were not sufficient to identify the type of heteroatom doping in the main electronic structure of C_3N_4. Similarly, the optical property results could not be used to identify the original and heteroatom-doped C_3N_4. Therefore, we are reporting on the identification of surface and bulk electronic properties using the RDB-PAS technique to generate ERDT patterns as a fingerprint of different doping elements in the C_3N_4 structure.

PXRD patterns of synthesized undoped C_3N_4 (CMN, CMA, and CDM), O-doped C_3N_4 (CU and CCA), and S-doped C_3N_4 (CT and CAT) photocatalysts from diverse precursors are presented in Fig. 1a. Diffraction peaks of all the synthesized catalysts can be observed at 2θ value of around 12.9°, due to the 100 plane,

[a] *Department of Earth Resources Engineering, Faculty of Engineering, Kyushu University, 744 Motooka, Nishiku, Fukuoka 819-0395, Japan. E-mail: keikos@mine.kyushu-u.ac.jp*
[b] *Department of Materials Science and Engineering, The Pennsylvania State University, University Park, Pennsylvania 16802, USA*
[c] *Institute for Catalysis, Hokkaido University, Sapporo 001-0021, Japan*
[d] *Department of Applied Chemistry, Faculty of Engineering, Kyushu University, 744 Motooka, Nishiku, Fukuoka 819-0395, Japan*
[e] *International Institute for Carbon-Neutral Energy Research (I2CNER), 744 Motooka, Nishiku, Fukuoka 819-0395, Japan*

† Electronic supplementary information (ESI) available. See DOI: 10.1039/c9cc09988c

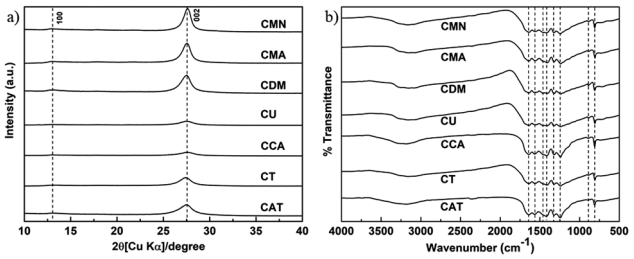

Fig. 1 (a) PXRD patterns, and (b) FTIR spectra of different heteroatom-doped C_3N_4.

corresponding to an interlayer stacking distance of aromatic units with d = 0.326 nm. The main diffraction peak, due to the 002 plane, appears at 2θ of about 27.6°, corresponding to an in-plane structural distance of C_3N_4 (d = 0.681 nm).[4] The heteroatom-doped C_3N_4 (CU, CCA, CT, and CAT) displayed lower intensity and broader diffraction peaks of the 002 plane than those of the undoped C_3N_4 (CMN, CMA, and CDM), indicating that the O- or S-containing precursors affected the crystallization and polymerization of C_3N_4 owing to strong C–O or C–S bonding, leading to defects in the final product.[5] However, no obvious 2θ differences were detected amongst the family of doped C_3N_4 samples, suggesting that they all contain a similar in-plane structural repeat motif and void-to-void distance (d = 0.681 nm).[6] This void-to-void distance was only slightly lower than that due to the collapsed structure of the tris-*s*-triazine unit (0.73 nm), which, for example, indexed 2θ peaks at 13.1° and 27.3°.[6] The FTIR spectra of C_3N_4 samples synthesized using the different precursors are presented in Fig. 1b. All samples showed similar spectra irrespective of whether O or S was present in the main structure (ESI†). Elemental compositions of C_3N_4 with and without heteroatom doping are summarized in Table S1 (ESI†). Around 2–3 wt% of O and 0.5–0.1 wt% of S were included in O-doped and S-doped C_3N_4, respectively.

The surface composition of undoped C_3N_4 and heteroatom-doped C_3N_4 was investigated by X-ray photoelectron spectroscopy (XPS). As shown in Fig. S2a (ESI†), the N 1s spectra of all samples were deconvoluted into four peaks at 398.5, 399.8, 402.4, and 405.9 eV, corresponding to sp^2 aromatic nitrogen bonded to carbon (C═N–C), tertiary nitrogen groups N(–C)$_3$, quaternary N in the aromatic rings, and π excitations, respectively. The O 1s spectra (Fig. S2b, ESI†) of undoped C_3N_4 and O-doped C_3N_4 were observed and separated into two peaks to confirm the presence of O in the synthetic samples. The peak at around 532 eV can be ascribed to C═O, while the peak centered at 534 eV can be attributed to surface-adsorbed water. To compare the O content in the different C_3N_4 samples, XPS surface sensitivity was calculated using N 1s and the peak area of C═O. The O-doped C_3N_4 clearly exhibits a higher O/N ratio than that of the undoped C_3N_4, indicating that O-doped C_3N_4 can be synthesized using urea and cyanuric acid (Table S2, ESI†). However, signals of the S 2p orbital in the S-doped C_3N_4 cannot be observed due to low S content in the samples.

The specific surface area (SSA) of the samples was obtained from N_2 adsorption–desorption measurements. The adsorption–desorption isotherms and SSAs of all samples are shown in Fig. S3 and Table S3 (ESI†), respectively. The O-doped C_3N_4 samples exhibit higher SSAs than the undoped C_3N_4, and S-doped C_3N_4, indicating that the destruction of the C_3N_4 skeleton occurred after O was doped into the main structure.[7]

The optical properties of undoped C_3N_4 and heteroatom-doped C_3N_4 were examined by ultraviolet-visible light (UV-vis) diffuse reflectance spectroscopy (DRS), as displayed in Fig. S4a (ESI†). All the photocatalysts exhibit high visible light absorption from 400 to 550 nm, indicating that the synthesized samples can be utilized as potential photocatalysts in the visible light region. In addition, the calculated energy bandgap (E_g) of all samples was calculated, as presented in Fig. S4b (ESI†). The E_g values of CMN, CMA, CDM, CU, CCA, CT, and CAT were estimated to be 2.77, 2.74, 2.76, 2.88, 2.92, 2.72, and 2.71 eV, respectively. CT and CAT (S-doped C_3N_4) display a lower E_g compared with CMN, CMA, and CDM (undoped C_3N_4), while CU and CCA (O-doped C_3N_4) show a higher E_g compared with undoped C_3N_4. This is a similar trend to in previous reports.[5,7–9] The red-shift in the absorption spectra to the more visible light region and decreasing E_g of CT and CAT enhance the light absorption in the visible light region, resulting in the generation of more electron–hole pairs which can improve the photocatalytic activity of the samples. In contrast, CU and CCA, which have low crystallinity and a thin-layer of C_3N_4, show a blue shift in the absorption spectra and a larger E_g than that of the undoped C_3N_4, which results from the quantum confinement effect.[7,10] The recombination of photogenerated electron–hole pairs of all of the photocatalysts was examined using photoluminescence spectroscopy. In Fig. S5 (ESI†), the undoped C_3N_4 (CMN, CMA, and CDM) show a higher photoluminescence intensity than that of O-doped C_3N_4 (CU and CCA) and S-doped C_3N_4 (CT and CAT), indicating that the heteroatom doping in the C_3N_4 structure can suppress electron and hole recombination.

Based on the PXRD, FTIR, and DRS results, it is difficult to classify the type of doping element in the C_3N_4 samples, which is related to photocatalytic activity. Thus, the newly developed characterization technique RDB-PAS was applied to study not only the surface structure but also the bulk electronic structure of the photocatalysts.[1,2] This study is the first instance to our knowledge applying RDB-PAS to the metal-free photocatalyst C_3N_4. ERDT patterns of all samples provided information about electron accumulation in electron traps (ETs) near the CBB, which indicated the ET levels in the samples. Surprisingly, synthesis of C_3N_4 from the different precursors, even if they have similar PXRD patterns and FTIR spectra, results in differently shaped ERDT patterns and total densities of ETs, as shown in Fig. 2. All the family of undoped C_3N_4 (CMN, CMA, and CDM), O-doped C_3N_4 (CU and CCA), and S-doped C_3N_4 (CT and CAT) display similar levels of accumulated electrons in the ETs around 2.7 eV near the CBB, which may be a characteristic of C_3N_4. However, the heteroatom-doped C_3N_4 (CU, CCA, CT, and CAT) produce different shapes of ERDT patterns from the undoped C_3N_4. The O-doped C_3N_4 (CU and CCA) present higher electron accumulation levels in the ETs at around 2.7 eV than that of the undoped C_3N_4, indicating an increase in total electron density in the ETs. In addition, new ETs at around 2.2 eV, which are created by the O/S impurities in the C_3N_4 structure, can be detected in the

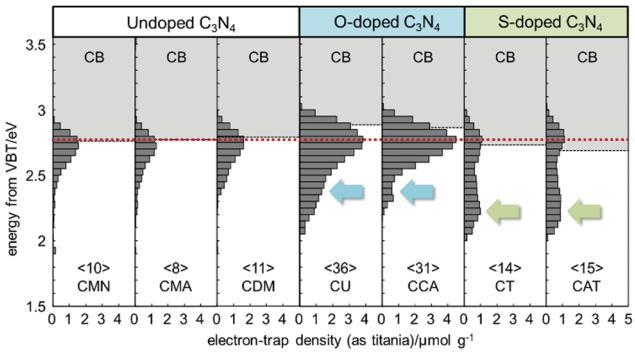

Fig. 2 ERDT patterns with CBB position of heteroatom-doped and undoped C_3N_4 photocatalysts. The number in ⟨ ⟩ denotes the total density of ETs, with the units of μmol g^{-1}. VBT, valence band top.

O-doped C_3N_4 and clearly observed in the S-doped C_3N_4. The changing ERDT pattern, total ET density, and CBB level after doping with O/S in C_3N_4 can be used to identify the type of doping element. To examine the similarities of synthesized C_3N_4 based on different heteroatom doping using different precursors, the overall degree of coincidence (ζ) of every pair of sample comparisons was calculated based on three factors: ERDT-pattern shape ($\zeta(a)$), total electron-trap density ($\zeta(b)$), and CBB position ($\zeta(c)$).[1] The $\zeta(c)$ value reflects the property of the bulk structure while $\zeta(a)$ and $\zeta(b)$ contribute to the surface structure property information on the "identicalness" or "similarity" without arbitrariness. The ζ of the photocatalyst can be evaluated using the following equation:

$$\zeta = \zeta(a) \times \zeta(b)^{\frac{1}{2}} \times \zeta(c)^2. \quad (1)$$

Table 1 shows the ζ for each sample pair. In comparison with CMN, the highest overall degree of coincidence (ζ) values are given by CMA and CDM owing to their high values of $\zeta(a)$ and $\zeta(b)$, which confirms the similarity of the undoped C_3N_4 samples. Moreover, the comparison between CU and CCA shows a high ζ value, while the comparison of CT and CAT also provides a high ζ value. Based on the ζ, the synthetic C_3N_4 samples from diverse precursors can be classified into three groups, undoped C_3N_4 (CMN, CMA, and CDM), O-doped C_3N_4 (CU and CCA), and S-doped C_3N_4 (CT and CAT), as the ζ value of each group samples is higher than 0.6, which suggests a high level of similarity for a pair of samples. Thus, the combination of ERDT and CBB (ERDT/CBB pattern) can be used as a fingerprint to identify the doping type of C_3N_4.

Furthermore, photocatalytic reduction of $Cr_2O_7^{2-}$ was performed to identify the effects of the doping elements related to the ERDT/CBB pattern, as shown in Fig. 3a and b. S-doped C_3N_4 (CT and CAT) showed a higher photocatalytic efficiency than undoped C_3N_4 (CMN, CMA, and CDM), while the photocatalytic activity and rate constants dramatically increased for O-doped C_3N_4 (CU and CCA). The improvement in the Cr(VI) reduction efficiency by O/S-doped C_3N_4 may be a reason for the enhancement of light absorption abilities, improved separation of photogenerated charge carriers, and an increase in SSAs,[11–13] in relation to increase in $\zeta(b)$. Moreover, the degree of coincidence for a photocatalytic reduction in Cr(VI) (ζ_{PC}) for each

Table 1 Summary of the degrees of coincidence (ζ) for different heteroatom-doped and undoped C_3N_4 photocatalysts

		CMN	CMA	CDM	CU	CCA	CT	CAT
CMN	$\zeta(a)$		0.88	0.79	0.50	0.68	0.14	0.11
	$\zeta(b)$		0.80	0.91	0.28	0.32	0.71	0.67
	$\zeta(c)$		0.99	1.00	0.96	0.95	0.98	0.98
	ζ		0.77	0.75	0.25	0.37	0.12	0.09
CMA	$\zeta(a)$	0.88		0.80	0.61	0.66	0.24	0.21
	$\zeta(b)$	0.80		0.73	0.22	0.32	0.71	0.67
	$\zeta(c)$	0.99		0.99	0.95	0.94	0.99	0.99
	ζ	0.77		0.68	0.27	0.35	0.20	0.17
CDM	$\zeta(a)$	0.79	0.80		0.64	0.76	0.22	0.22
	$\zeta(b)$	0.91	0.73		0.31	0.35	0.79	0.73
	$\zeta(c)$	1.00	0.99		0.96	0.95	0.99	0.98
	ζ	0.75	0.68		0.34	0.43	0.20	0.19
CU	$\zeta(a)$	0.50	0.61	0.64		0.70	0.59	0.60
	$\zeta(b)$	0.28	0.22	0.31		0.86	0.39	0.42
	$\zeta(c)$	0.96	0.95	0.96		0.99	0.94	0.94
	ζ	0.25	0.27	0.34		0.64	0.35	0.37
CCA	$\zeta(a)$	0.68	0.66	0.76	0.70		0.47	0.49
	$\zeta(b)$	0.32	0.32	0.35	0.86		0.45	0.48
	$\zeta(c)$	0.95	0.94	0.95	0.99		0.93	0.93
	ζ	0.37	0.35	0.43	0.64		0.29	0.31
CT	$\zeta(a)$	0.14	0.24	0.22	0.59	0.47		0.88
	$\zeta(b)$	0.71	0.71	0.79	0.39	0.45		0.93
	$\zeta(c)$	0.98	0.99	0.99	0.94	0.93		1.00
	ζ	0.12	0.20	0.20	0.35	0.29		0.85
CAT	$\zeta(a)$	0.11	0.21	0.22	0.60	0.49	0.88	
	$\zeta(b)$	0.67	0.67	0.73	0.42	0.48	0.93	
	$\zeta(c)$	0.98	0.99	0.98	0.94	0.93	1.00	
	ζ	0.09	0.17	0.19	0.37	0.31	0.85	

sample pair was calculated to elucidate the relationship between ERDT/CBB patterns and the photocatalytic Cr(VI) reduction (Table S4, ESI†). High ζ_{PC} (>0.9) for CU and CCA can be observed along with a high value of ζ (>0.6), while a low value of ζ provides a low ζ_{PC}, indicating that the ζ of the ERDT/CBB pattern induces ζ_{PC}. Moreover, each sample group (undoped C_3N_4, O-doped C_3N_4 and S-doped C_3N_4) with high ζ shows high similarity of photocatalytic Cr(VI) reduction efficiency. Thus, the photocatalytic activity of undoped and doped C_3N_4 can be predicted by checking ζ of the ERDT/CBB pattern. If sample pairs showed $\zeta \geq 0.6$, they might have identical photocatalytic performances ($\zeta_{PC} \geq 0.9$). The ERDT/CBB patterns from the RDB-PAS technique can be used not only to identify the different types of heteroatom doping in C_3N_4 (instead of using the traditional techniques PXRD and FTIR) but also to predict photocatalytic performance. For the reduction mechanism of Cr(VI) with visible-light illumination, C_3N_4 produces photogenerated electron–hole

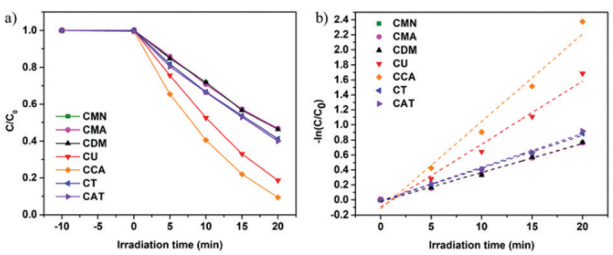

Fig. 3 (a) Photocatalytic reduction of Cr(VI), and (b) kinetics plots for the heteroatom-doped and undoped C_3N_4 photocatalysts at different time intervals.

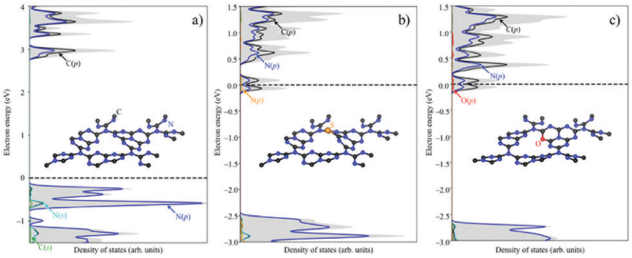

Fig. 4 Projected state densities of (a) C_3N_4, (b) S-doped C_3N_4, and (c) O-doped C_3N_4. Doping of S and O in C_3N_4 causes the formation of mid-gap states that are close to the conduction band.

pairs by absorbing photon energy.[14] The photogenerated electrons can be easily transferred to the C_3N_4 surface and accumulated in new donor levels near the CBB interface; subsequently, the excited electron can reduce the $Cr_2O_7^{2-}$ to Cr^{3+} on the C_3N_4 surface. The suppression of electron–hole pair recombination and charge transfer by heteroatom-doped C_3N_4, which was confirmed by photoluminescence (PL), electrochemical impedance spectroscopy (EIS) and time-resolved photoluminescence (TRPL) (Fig. S6a, b and Table S5, ESI†), produces improvement of photocatalytic Cr(VI) reduction activity.

To confirm the location of S and O in the C_3N_4 structure and the electronic states generated by the guest elements, electronic-structure calculations were performed at the Perdew–Burke–Ernzerhof (PBE) semi-local level of density-functional theory[15] using the projected augmented wave method implemented in the Vienna Ab-initio Simulation Package (VASP).[16] The substitutions of nitrogen at three different S and O positions in the C_3N_4, center, edge, and connection, are denoted as N_{center}, N_{edge}, and $N_{connect}$, respectively, and are shown in Fig. S7 (ESI†). The substitution energies of S (ΔE_S) at N_{center}, N_{edge}, and $N_{connect}$ were calculated to be 2.20 eV, 0.92 eV, and 1.84 eV, respectively, indicating that N_{edge} is the preferential doping site for S. Similarly, oxygen substitution is favored at N_{edge}, with substitution energy O (ΔE_O) of −0.32 eV, −1.15 eV, and 0.32 eV at the N_{center}, N_{edge}, and $N_{connect}$ sites, respectively. We thus adopt N_{edge} substitution as the relevant doping geometry for subsequent projected density of states (PODS) calculations as shown in Fig. 4. It is clear that the valence band (VB) and conduction band (CB) of undoped C_3N_4 (CMN, CMA, and CDM), O-doped C_3N_4 (CU and CCA), and S-doped C_3N_4 (CT and CAT) are dominated by the p orbitals of N and C. Importantly, the substitutional doping of S and O induces mid-gap states that are close to the CB, as shown in Fig. 4b and c. These results confirm the generation of intermediate electronic levels after doping S and O into C_3N_4 structures, corresponding to the observation of ET levels in the ERDT/CBB patterns of the heteroatom-doped C_3N_4 samples.

In summary, this work provides a new method to characterize and classify C_3N_4 both with and without heteroatom doping using RDB-PAS. The ERDT patterns, which were obtained using RDB-PAS, along with the CBB, were significantly influenced by the doped atoms but not affected by the precursors of C_3N_4. The different heteroatom-doped C_3N_4 samples showed different ERDT/CBB pattern shapes, which could be used to identify the similarities or differences in the family of C_3N_4 photocatalysts. The samples in each group of undoped C_3N_4 (CMN, CMA, and CDM), O-doped C_3N_4 (CU and CCA), and S-doped C_3N_4 (CT and CAT) exhibited similar ζ values calculated from the ERDT/CBB patterns, confirming that samples of C_3N_4 doped with the same atoms produce similar ERDT/CBB pattern shapes and $\zeta(b)$ values. Moreover, the photocatalytic Cr(VI) reduction performances of differently doped C_3N_4 samples were related to their ERDT/CBB patterns. Thus, the ERDT/CBB analysis can be used as an alternative method to identify the doping element in a C_3N_4 sample and its photocatalytic efficiency.

This work was supported by the Japan Society for the Promotion of Science (JSPS) KAKENHI Grants no. JP17F17355 and JP18F18387, the Cooperative Research Programs at Hokkaido University Institute for Catalysis (no. 18A1001 and 19B1002) and ''Progress 100'' (World Premium International Researcher Invitation Program) at Kyushu University through operating expense grants of the Ministry of Education, Culture, Sports, Science and Technology. ID and YX acknowledge financial support from the National Science Foundation under Grant no. DMREF-1729338. Part of this work was conducted at Kyushu University, supported by the Nanotechnology Platform Program (Molecule and Material Synthesis) of the Ministry of Education, Culture, Sports, Science and Technology (MEXT), Japan.

Conflicts of interest

The authors declare that there is no conflict of interest.

Notes and references

1 A. Nitta, M. Takase, M. Takashima, N. Murakami and B. Ohtani, *Chem. Commun.*, 2016, **52**, 12096–12099.
2 A. Nitta, M. Takashima, N. Murakami, M. Takase and B. Ohtani, *Electrochim. Acta*, 2018, **264**, 83–90.
3 P. Ketwong, M. Takashima, A. Nitta, P. Pookmanee and B. Ohtani, *J. Environ. Chem. Eng.*, 2018, **6**, 2048–2054.
4 X. Wang, K. Maeda, A. Thomas, K. Takanabe, G. Xin, J. M. Carlsson, K. Domen and M. Antonietti, *Nat. Mater.*, 2009, **8**, 76–80.
5 M. Ismael, Y. Wu, D. H. Taffa, P. Bottke and M. Wark, *New J. Chem.*, 2019, **43**, 6909–6920.
6 A. Thomas, A. Fischer, F. Goettmann, M. Antonietti, J. O. Muller, R. Schlogl and J. M. Carlsson, *J. Mater. Chem.*, 2008, **18**, 4893–4908.
7 Y. Wang, L. Rao, P. Wang, Y. Guo, X. Guo and L. Zhang, *Environ. Sci. Pollut. Res. Int.*, 2019, **26**, 15710–15723.
8 K. Wang, Q. Li, B. S. Liu, B. Cheng, W. K. Ho and J. G. Yu, *Appl. Catal., B*, 2015, **176**, 44–52.
9 Y. Luo, J. Wang, S. Yu, Y. Cao, K. Ma, Y. Pu, W. Zou, C. Tang, F. Gao and L. Dong, *J. Mater. Res.*, 2018, **33**, 1268–1278.
10 X. Zhang, X. Xie, H. Wang, J. Zhang, B. Pan and Y. Xie, *J. Am. Chem. Soc.*, 2013, **135**, 18–21.
11 R. Tang, R. Ding and X. Xie, *Water Sci. Technol.*, 2018, **78**, 1023–1033.
12 J. Li, B. Shen, Z. Hong, B. Lin, B. Gao and Y. Chen, *Chem. Commun.*, 2012, **48**, 12017–12019.
13 G. Mamba and A. K. Mishra, *Appl. Catal., B*, 2016, **198**, 347–377.
14 A. Ali, X. D. Li, J. L. Q. Song, S. Y. Yang, W. T. Zhang, Z. M. Zhang, R. X. Xia, L. X. Zhu and X. L. Xu, *J. Phys. Chem. C*, 2017, **121**, 21096–21104.
15 J. P. Perdew, K. Burke and M. Ernzerhof, *Phys. Rev. Lett.*, 1996, **77**, 3865–3868.
16 G. Kresse and J. Furthmuller, *Phys. Rev. B: Condens. Matter Mater. Phys.*, 1996, **54**, 11169–11186.

